

## HALO MASS FUNCTIONS AT HIGH REDSHIFT

HANNAH O'BRENNAN<sup>1,\*</sup>, JOHN A. REGAN<sup>1</sup>, CHRIS POWER<sup>2,3</sup>, SAOIRSE WARD<sup>1</sup>, JOHN BRENNAN<sup>1</sup>, AND JOE MCCAFFREY<sup>1</sup>

<sup>1</sup>Centre for Astrophysics and Space Science Maynooth, Department of Physics, Maynooth University, Maynooth, Ireland

<sup>2</sup>International Centre for Radio Astronomy Research (ICRAR), M468, University of Western Australia, 35 Stirling Hwy, Crawley, WA 6009, Australia

<sup>3</sup>ARC Centre of Excellence for All Sky Astrophysics in 3 Dimensions (ASTRO 3D)

Version November 26, 2025

### ABSTRACT

Recent JWST observations of very early galaxies, at  $z \gtrsim 10$ , have led to claims that tension exists between the sizes and luminosities of high-redshift galaxies and what is predicted by standard  $\Lambda$ CDM models. Here we use the adaptive mesh refinement code **Enzo** and the N-body smoothed particle hydrodynamics code **SWIFT** to compare (semi-)analytic halo mass functions against the results of direct N-body models at high redshift. In particular, our goal is to investigate the variance between standard halo mass functions derived from (semi-)analytic formulations and N-body calculations and to determine what role any discrepancy may play in driving tensions between observations and theory. We find that the difference between direct N-body calculations and (semi-) analytic halo mass function fits is less than a factor of 2 (at  $z \sim 10$ ) within the mass range of galaxies currently being observed by JWST, and is therefore not a dominant source of error when comparing theory and observation at high redshift.

### 1. INTRODUCTION

Since its launch in December 2021 and its subsequent data releases in the months since, JWST has both reshaped and challenged our understanding of galaxy formation in the very early Universe ( $z \gtrsim 10$ ). In particular, JWST has discovered a number of very massive and very luminous galaxies at redshifts in excess of  $z = 10$  which, after initial photometric detection, have now been spectroscopically confirmed (Harikane et al. 2024; Arrabal Haro et al. 2023a; Castellano et al. 2024; Hainline et al. 2024; Gentile et al. 2024). These galaxies, both in terms of their intrinsic luminosity and their potential host halo masses, provide a significant challenge to our understanding of structure formation in the early Universe. Boylan-Kolchin (2023), using an analytic model applied to the inferred JWST stellar masses of a number of high-redshift sources from Labbé et al. (2023), found that the stellar masses implied by the sources required star formation efficiencies,  $\epsilon$ , significantly in excess of those from the present-day universe and perhaps as implausibly high as  $\epsilon = 1$ . The model employed by Boylan-Kolchin (2023) hinges on a number of simple yet strong assumptions. These assumptions use the inferred stellar host mass to derive a host halo mass based on the ratios between the cosmic baryon density and the cosmic matter density and the star formation efficiency. These simple arguments culminate in a calculation of the probability of finding such (luminous) galaxies at early times in a  $\Lambda$ CDM universe.

Boylan-Kolchin (2023) conclude that the most massive JWST galaxies detected are both at the very limit of galaxy formation theory and that their number densities are difficult to equate with the JWST field of view. They conclude that these issues indicate that there are several unresolved issues in our theories. However, underneath the model employed by Boylan-Kolchin (2023) are

a number of astrophysical assumptions which are used when converting the broadband spectral energy distribution to a host stellar mass. This conversion is open to large uncertainties - particularly since our knowledge of how to do this conversion comes from the local Universe. There is no guarantee that these conversion relations can be directly mapped to the high- $z$  Universe and in fact most analysis shows that it is almost certainly not the case (e.g. Kannan et al. 2023; Lu et al. 2024). For example, recent analysis by Steinhardt et al. (2023) show that modifying the host population IMF of the inferred stellar population results in a decrease in the stellar mass by factors of between 10 and 50. Such decreases in the host stellar mass have a direct knock-on effect to the inferred host halo mass and can significantly decrease the tension with  $\Lambda$ CDM models.

Adding to this important point is that Boylan-Kolchin (2023) (as well as many other studies) utilise the well-tested and parameterised halo mass function (HMF) derived by Sheth & Tormen (1999) in order to compute their galaxy number densities and cumulative comoving number density of galaxies. An important consideration therefore is to test, using explicit N-body calculations, how accurate the underlying HMF is at high- $z$  (i.e. at  $z \gtrsim 10$ ), compared to direct N-body calculations, and what error may be associated with this model. This is the goal of this study.

While preparing this work a study by Yung et al. (2024) performed a similar investigation. Using a high-fidelity suite of N-body simulations across a broad range of box sizes and redshifts, Yung et al. (2024) were able to show that HMFs derived from fitting functions and analytical approximations match extremely well to their N-body simulations. Yung et al. (2024) found that even up to  $z = 15$  the match between their N-body simulations and the fitting functions is no more than approximately a factor of two across a range of fitting functions. As discussed above, providing robust quantification of the

\*E-mail:hannah.obrennan.2021@mumail.ie

$L$ [cMpc/h]	$N_{\text{DM}}^{1/3}$	$M_{\text{DM}}$ [ $M_{\odot}/h$ ]
0.5	512	$6.69 \times 10^1$
1.5	512	$1.81 \times 10^3$
2.5	512	$8.37 \times 10^3$
7.5	1024	$2.83 \times 10^4$
7.5	512	$2.26 \times 10^5$
12.5	1024	$1.31 \times 10^5$
12.5	512	$1.05 \times 10^6$
25.0	1024	$1.05 \times 10^6$
25.0	512	$8.37 \times 10^6$
50.0	1024	$8.37 \times 10^6$
50.0	512	$6.70 \times 10^7$
100.0	1024	$6.70 \times 10^7$
100.0	512	$5.36 \times 10^8$

TABLE 1

MASS RESOLUTIONS OF EACH SIMULATION BOX. ALL SIMULATIONS BUT THE  $L = 7.5$  cMpc/h,  $N_{\text{DM}}^{1/3} = 1024$  BOX ARE RUN USING BOTH **Enzo** AND **SWIFT**; THIS BOX IS RUN USING **SWIFT** ONLY.

match between fitting functions and direct N-body calculations at high- $z$  is extremely timely given the recent JWST results.

This is particularly relevant when trying to understand the probability of finding such luminous and massive galaxies within a JWST field of view. Thus far several studies have tested the first results from JWST against state-of-the-art hydrodynamical simulations and the results agree within a factor of a few (e.g. Keller et al. 2023; McCaffrey et al. 2023; Sun et al. 2023; Rennehan 2024). It is therefore timely to quantify potential sources of systematic error when comparing observations and models.

Here we perform a similar analysis to Yung et al. (2024), with the difference being that we compare HMF fitting functions against two fundamentally different numerical codes - **Enzo** (Bryan et al. 2014; Brummel-Smith et al. 2019) and **SWIFT** (Schaller et al. 2018, 2024). While Yung et al. (2024) used the publicly available Gadget-2 code (Springel 2005) which is a TreePM code, with a similar gravitational solver to **SWIFT**, we also use the Particle-Mesh based **Enzo** code which gives an additional layer of comparison. Our analysis confirms the results of Yung et al. (2024) and we also observe a factor of approximately two difference between the HMFs generated by the N-body codes and the fitting functions.

The structure of the paper is as follows: In §2 we outline the methodology including the simulations and fitting functions employed. In §3 we deliver the results of our analysis and in §4 we summarize and discuss our results in light of recent JWST observations.

## 2. METHODOLOGY

### 2.1. Numerical simulations

We run a series of dark matter-only simulations using **Enzo** and **SWIFT** of varying resolutions, achieved by varying both the box size and particle number. The box size varies from  $L = 0.5$  cMpc/h to 100.0 cMpc/h and the particle number varies from  $N_{\text{DM}} = 512^3$  to  $1024^3$ . Details of the simulation boxes are summarised in Tables 1 and 2.

Our simulations begin at  $z = 127.0$  with initial conditions set using MUSIC (Hahn & Abel 2011) and end at  $z = 10.0$ . We use a  $\Lambda$ CDM cosmology with  $h = 0.6774$ ,  $\Omega_{\text{m},0} = 0.2592$ ,  $\sigma_8 = 0.8159$ ,  $n_{\text{eff}} = 0.9667$  and the Eisenstein & Hu (1998) transfer function for no baryon

$L$ [cMpc/h]	$N_{\text{DM}}^{1/3}$	$\Delta x_{\text{Enzo}}$ [cpc/h]	$\Delta x_{\text{SWIFT}}$ [cpc/h]
0.5	512	$7.63 \times 10^0$	$3.91 \times 10^1$
1.5	512	$2.29 \times 10^1$	$1.17 \times 10^2$
2.5	512	$3.82 \times 10^1$	$1.95 \times 10^2$
7.5	1024	-	$2.93 \times 10^2$
7.5	512	$1.14 \times 10^2$	$5.86 \times 10^2$
12.5	1024	$9.54 \times 10^1$	$4.88 \times 10^2$
12.5	512	$1.91 \times 10^2$	$9.77 \times 10^2$
25.0	1024	$1.91 \times 10^2$	$9.77 \times 10^2$
25.0	512	$3.82 \times 10^2$	$1.95 \times 10^3$
50.0	1024	$3.82 \times 10^2$	$1.95 \times 10^3$
50.0	512	$7.63 \times 10^2$	$3.91 \times 10^3$
100.0	1024	$7.63 \times 10^2$	$3.91 \times 10^3$
100.0	512	$1.53 \times 10^3$	$7.81 \times 10^3$

TABLE 2

HIGHEST SPACE RESOLUTIONS OF EACH SIMULATION BOX. ALL SIMULATIONS BUT THE  $L = 7.5$  cMpc/h,  $N_{\text{DM}}^{1/3} = 1024$  BOX ARE RUN USING BOTH **Enzo** AND **SWIFT**; THIS BOX IS RUN USING **SWIFT** ONLY.

acoustic oscillations. The two codes we use, **Enzo** and **SWIFT**, are both well-tested and have been used extensively within the community. Additionally, both codes use somewhat different strategies for solving the Poisson equation which allows for additional comparison between the various semi-analytic fits against numerical solutions. We now describe both codes but refer the interested reader to the code method papers for more details.

**Enzo** is a grid-based N-body code with the capability for adaptive mesh refinement (AMR), widely used in cosmological hydrodynamics simulations. The AMR allows for improved resolution in areas of interest (e.g. collapsing structures) without greatly increasing computational cost and without needing prior knowledge of the volume to pre-select areas for increased refinement. The gravity solver works by implementing a Fast Fourier Transform (FFT) technique to solve Poisson's equation at the root grid of each timestep of the simulation. The boundary conditions on the subgrids are then interpolated from the parent grid and the Poisson equation is solved at each time step, one subgrid at a time. For a unigrid **Enzo** simulation (i.e. no refinement), the minimum inter-particle separation in which gravity acts is twice the length of two cells, given as:

$$\Delta x_{\text{Unigrid}} = 2 \frac{L}{N_{\text{DM}}^{1/3}}. \quad (1)$$

When running **Enzo** simulations, we used a maximum refinement level of 8, meaning that the resolution was increased by a factor  $2^8$  in regions of high particle density. This means the highest resolution is given as:

$$\Delta x_{\text{Enzo}} = \frac{1}{2^8} \Delta x_{\text{Unigrid}} = \frac{1}{2^7} \frac{L}{N_{\text{DM}}^{1/3}}. \quad (2)$$

For the dark matter-only simulations carried out here, refinement is triggered once the particle overdensity reaches a factor of 4 greater than the mean density (i.e. `MinimumOverDensityForRefinement` = 4). In addition to this we set the `MinimumMassForRefinementLevelExponent` = -0.1 which makes the refinement scheme super-Lagrangian and allows for the higher levels of refinement to be more easily triggered. The combination of these parameter

choices mean that our simulation setup is somewhat conservative, employing an aggressive refinement strategy (see e.g. O’Shea et al. 2005).

*SPH With Inter-dependent Fine-grained Tasking - SWIFT* - combines a tree-based N-body solver with a smoothed particle hydrodynamics (SPH) solver. In this study, we use the adaptive mode of the Fast Multipole Method (FMM) (Cheng, Greengard & Rokhlin (1999)). This implements a Taylor expansion twice to resolve the gravitational potential (and later the forces) between particles in different cells. We set the accuracy criterion  $\epsilon_{\text{FMM}} = 0.001$ . *SWIFT* takes advantage of the hierarchical tree structure to efficiently solve for the gravitational forces between particles. Particles from nearest neighbour cells are treated as individuals. A group of particles from distant cells are approximated as one particle with the total mass of the group located at the centre of mass. Long-range forces are resolved using a Fast Fourier Transform algorithm (Frigo & Johnson (2005)).

It is a non-trivial matter comparing *Enzo* and *SWIFT* due to the difference in the gravity solvers. The highest spatial resolution for an *Enzo* simulation,  $\Delta x_{\text{Enzo}}$ , applies only to regions of high particle density. The softening length for a *SWIFT* simulation,  $\Delta x_{\text{SWIFT}}$ , applies to the entire simulation volume. We compromise by setting the softening length to an intermediate value, between  $\Delta x_{\text{Unigrid}}$  and  $\Delta x_{\text{Enzo}}$ :

$$\Delta x_{\text{SWIFT}} = \frac{1}{5^2} \frac{L}{N_{\text{DM}}^{1/3}}. \quad (3)$$

## 2.2. Numerical Halo Finders

As discussed in §1 the goal of this paper is to determine the differences between (semi-)analytic HMFs and those derived from direct N-body simulations. In order to determine the HMF from the cosmological simulations we must employ a halo finder and decide on the redshifts at which to evaluate the HMFs.

We analyse the simulation snapshots from our full suite of outputs at  $z = 20.0$ ,  $z = 15.0$  and  $z = 10.0$  using a friends-of-friends (FOF) (Efstathiou et al. (1985)) and HOP halo (Eisenstein & Hut (1998)) finder (results from the HOP finder can be found in the appendix of the paper as the results are very similar between FOF and HOP and the goal of this study is not to compare halo finders). The FOF halo finder accounts for the distances between dark matter particles within a single snapshot. We use a linking length  $\Delta x(b) = b \times L/N_{\text{DM}}^{1/3}$ , where  $L/N_{\text{DM}}^{1/3}$  is the mean inter-particle separation. This refers to the maximum permitted separation between two particles. A group i.e. halo is found from a set of inter-linked particles.

Our halos are approximated as spheres and ideally, we choose  $b$  such that each halo encompasses a volume with an overdensity  $\Delta_c \approx 18\pi^2$  i.e. 178 times the critical density  $\rho_c(z)$  (Bryan & Norman (1998)). The Python package *hmf* (Murray, Power & Robotham 2013) provides an approximation relating  $\Delta_c$  and  $b$ :

$$\Delta_c(z) = \frac{9}{2\pi b^3} \Omega_m(z). \quad (4)$$

As  $z \rightarrow \infty$ ,  $\Omega_m(z) \rightarrow 1$  in our cosmology. Therefore,  $b = 0.2$  results in a predicted overdensity of  $\Delta_c \approx 178$

and this is the value we choose for our FOF algorithm.

The HOP halo finder accounts for the distances between particles as well as the computed density of each particle. Rather than creating a continuous density field in the simulation volume, the density of each particle at its given position is estimated using a spherically symmetric cubic spline kernel (Monaghan & Lattanzio (1985)) on its  $N_{\text{dens}} = 64$  nearest neighbours. The density is normalised to the average density of particles within the simulation box e.g. a particle with a computed density of  $\delta = 80$  refers to a position 80 times denser than the average i.e. an overdensity (Skory et al. (2010)). A link is made by hopping from a given particle to the densest of its  $N_{\text{hop}} = 64$  neighbours. This process continues, forming a chain of increasing particle density until we reach a particle that is its own densest neighbour. All chains sharing the same densest particle are part of the same group. If the maximum particle density within a group is above a set threshold overdensity  $\delta_{\text{peak}}$ , that group is defined as a halo. We use a threshold overdensity of  $\delta_{\text{peak}} = 100$ . This value was chosen to calibrate the HOP finder with the FOF finder so both halo finders found a similar halo number and mass range for the *Enzo*,  $L = 0.5$  cMpc/h,  $N_{\text{DM}} = 512^3$ ,  $z = 10$  snapshot.

The halo masses found from these halo catalogues are the FOF and HOP masses i.e. the mass of the halo is defined as the sum of the masses of the particles that make up the halos. After we create halo catalogues based on these halo finders, we only include halos made up of at least  $N_{\text{DM}, \text{min}} = 100$  particles to reduce numerical over-counting (i.e. halos must be well resolved (by at least 100 particles) before we identify them as halos).

We find that there is little difference between the number densities found using FOF and HOP for a given simulation suite, with HOP underestimating the FOF number densities by a factor of  $\approx 2$  at most (see Figure 1 for a comparison). Given that the halo finder parameters were calibrated at  $z = 10.0$ , it is not surprising that there is little mass variance in their number density ratio at this redshift. From this point onwards we show the results for FOF only and leave those from HOP to the appendix.

## 2.3. Numerical Halo Number Densities

A halo catalogue is created from each snapshot with a specific halo finder using the *yt*<sup>1</sup> and *yt-astro-analysis* packages (Turk et al. (2011), Smith et al. (2022)). An array of halo mass values is generated from each halo catalogue, filtered to exclude halos consisting of  $< N_{\text{DM}, \text{min}}$  particles. For each array, the halo mass values are binned on a logarithmic scale into 24 histogram bins with  $M_{\text{min}} = 10^{3.75} M_{\odot}/h$  and  $M_{\text{max}} = 10^{11.75} M_{\odot}/h$ . Halo catalogues from a given simulation suite, halo finder and redshift,  $z$ , are combined, giving rise to 12 datasets (see Table 3 for more detail). For each *Enzo* dataset, we combine halo catalogues based on 12 simulation boxes. For each *SWIFT* dataset, we combine halo catalogues based on 13 simulation boxes (see Tables 1 and 2 for more detail). In our algorithm below, we index datasets with  $i \in \{1, \dots, 12\}$ ,

<sup>1</sup> We use a version of *yt* called *yt-swift* developed by Rennehan (2022) as the most recently available version of *yt* cannot load *SWIFT* output data.

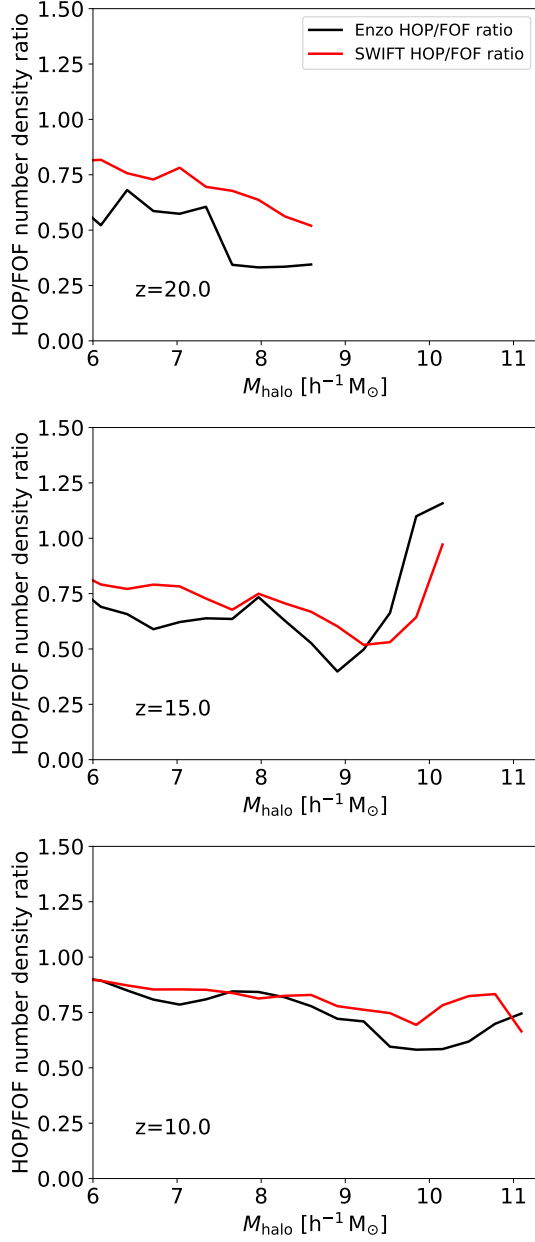


FIG. 1.— Comparing the FOF and HOP halo number densities derived from **Enzo** and **SWIFT** simulation data (with halo masses on a logarithmic scale). We show how the ratio of the HOP number density to the FOF number density varies with halo mass. The HOP number density is within a factor of 2 of its FOF counterpart - particularly at the  $z = 10$  outputs. Some larger deviations at higher  $z$  are seen as expected.

mass bins with  $j \in \{1, \dots, 24\}$ , **Enzo** simulation boxes with  $k \in \{1, \dots, 12\}$ , and **SWIFT** simulation boxes with  $k \in \{1, \dots, 13\}$ .

For example, consider the  $i = 3$  dataset (**Enzo**, FOF,  $z = 10.0$ ). Say we wish to find the number density  $n_{\text{halo}, i=3}^{\text{num}}(M_{\text{mid}, j})$  of the  $j^{\text{th}}$  bin centred at some mass  $\log_{10}(M_{\text{mid}, j}/h^{-1} M_{\odot})$ . We count the number of halos  $N_{\text{halo}, 3, j, k}$  in this bin for each simulation box  $\forall k = 1, \dots, 12$  and this specific halo number density is given as:

$$n_{\text{halo}, 3, j, k}^{\text{num}}(M_{\text{mid}, j}) = \frac{N_{\text{halo}, 3, j, k}}{V_k}, \quad (5)$$

Simulation	Halo finder	Snapshot Redshift ( $z$ )
<b>Enzo</b>	FOF	20.0
		15.0
		10.0
	HOP	20.0
<b>SWIFT</b>	FOF	20.0
		15.0
		10.0
	HOP	20.0
		15.0
		10.0

TABLE 3  
THE 12 DATASETS DERIVED BY COMBINING HALO CATALOGUES FOR EACH SIMULATION, HALO FINDER, AND REDSHIFT COMBINATION.

where  $V_k$  is the comoving volume of the  $k^{\text{th}}$  simulation box.

We find the halo number density  $n_{\text{halo}, 3}^{\text{num}}(M_{\text{mid}, j})$  by averaging over all non-zero number densities across all 12 simulation boxes:

$$n_{\text{halo}, 3}^{\text{num}}(M_{\text{mid}, j}) = \frac{1}{S_{3,j}} \sum_k n_{\text{halo}, 3, j, k}^{\text{num}}(M_{\text{mid}, j}), \quad (6)$$

where  $S_{3,j}$  is the number of halo catalogues that found a non-zero halo number density for the  $j^{\text{th}}$  bin in this dataset.

We can generalise the above equation for the  $i^{\text{th}}$  dataset and  $j^{\text{th}}$  bin as:

$$n_{\text{halo}, i}^{\text{num}}(M_{\text{mid}, j}) = \frac{1}{S_{i,j}} \sum_k n_{\text{halo}, i, j, k}^{\text{num}}(M_{\text{mid}, j}). \quad (7)$$

#### 2.4. (Semi-)Analytical Halo Mass Functions

We compare our numerical halo number densities with those derived from both analytical forms and popular fits. The number density (units:  $h^3 \text{ cMpc}^{-3}$ ) of dark matter halos at a given redshift,  $z$ , in a mass bin centred at  $\log_{10}(M_{\text{mid}}/h^{-1} M_{\odot})$  with a width of  $\Delta \log_{10} M$  is defined as:

$$n_{\text{halo}}^{\text{fit}}(z, M_{\text{mid}}) = \int_{M_a(M_{\text{mid}})}^{M_b(M_{\text{mid}})} \frac{dn}{dM}(z, M) dM, \quad (8)$$

$$\log_{10} M_a(M_{\text{mid}}) = \log_{10} \left( \frac{M_{\text{mid}}}{h^{-1} M_{\odot}} \right) - \frac{\Delta \log_{10} M}{2},$$

$$\log_{10} M_b(M_{\text{mid}}) = \log_{10} \left( \frac{M_{\text{mid}}}{h^{-1} M_{\odot}} \right) + \frac{\Delta \log_{10} M}{2}.$$

The halo mass function (units:  $h^4 \text{ cMpc}^{-3} M_{\odot}^{-1}$ ) is the differential halo number density per unit mass and is defined as:

$$\frac{dn}{dM}(z, M) = \frac{\rho_0}{M^2} f(\sigma(z, M)) \left| \frac{d \ln \sigma(z, M)}{d \ln M} \right|. \quad (9)$$

Here  $\rho_0$  (units:  $h^2 M_{\odot} \text{ cMpc}^{-3}$ ) and  $\sigma(z, M)$  refer to



the mean density of the universe and mass variance respectively. The mass variance is given as:

$$\sigma^2(z, M) = \frac{1}{2\pi^2} \int_0^\infty k^2 P(z, k) \tilde{W}^2(kR(M)) dk, \quad (10)$$

where  $P(z, k)$  is the linear power spectrum and  $\tilde{W}(kR)$  is a window function with a filter defined by  $R = R(M)$ . We use the Top Hat window function given as:

$$\tilde{W}(kR) = \frac{3}{(kR)^3} [\sin(kR) - (kR) \cos(kR)], \quad (11)$$

$$W(r) = \begin{cases} \frac{3}{4\pi R^3} & \text{if } r < R \\ 0 & \text{if } r > R. \end{cases} \quad (12)$$

The linear power spectrum evolves with  $z$  as:

$$P(z, k) = d(a(z))^2 P(z=0, k), \quad (13)$$

where  $a(z) = 1/(1+z)$  and  $d(a)$  is the normalised linear growth factor (Lukić et al. (2007)) given as:

$$d(a) = \frac{D^+(a)}{D^+(a=1)}, \quad (14)$$

$$D^+(a) = \frac{5\Omega_{m,0}}{2} \frac{H(a)}{H_0} \int_0^a \frac{da'}{[a'H(a')/H_0]^3}. \quad (15)$$

The exact form of  $P(z=0, k)$  depends on the cosmology and the choice of transfer function. Like with our simulations, we initialise the `hmf` objects with the Eisenstein & Hu (1998) transfer function with no baryon acoustic oscillations. The exact form of  $f(\sigma(z, M))$  depends on the choice of fitting function for the halo mass function.

#### 2.4.1. Press-Schechter Theory

In Press & Schechter (1974) (PS), a spherical collapse model is assumed for dark matter halos and the probability of reaching a threshold density field value follows a Gaussian distribution. Thus the fitting function for PS is given as:

$$f_{\text{PS}}(\sigma) = \sqrt{\frac{2}{\pi}} \frac{\delta_c}{\sigma} \exp\left(-\frac{\delta_c^2}{2\sigma^2}\right), \quad (16)$$

where  $\delta_c \approx 1.686$  is the critical overdensity required for a region to spherically collapse into a dark matter halo. A limitation of the PS fitting function is its tendency to overestimate the number of lower-mass halos and underestimate the number of higher-mass halos compared to N-body simulations (Lacey & Cole (1994), Sheth & Tormen (1999)). Since this seminal paper, many other fitting functions have been developed that aim to correct for this discrepancy as well as attempting to add additional sophistication to the modelling. In this work, we explore four other halo mass fitting functions in addition to PS.

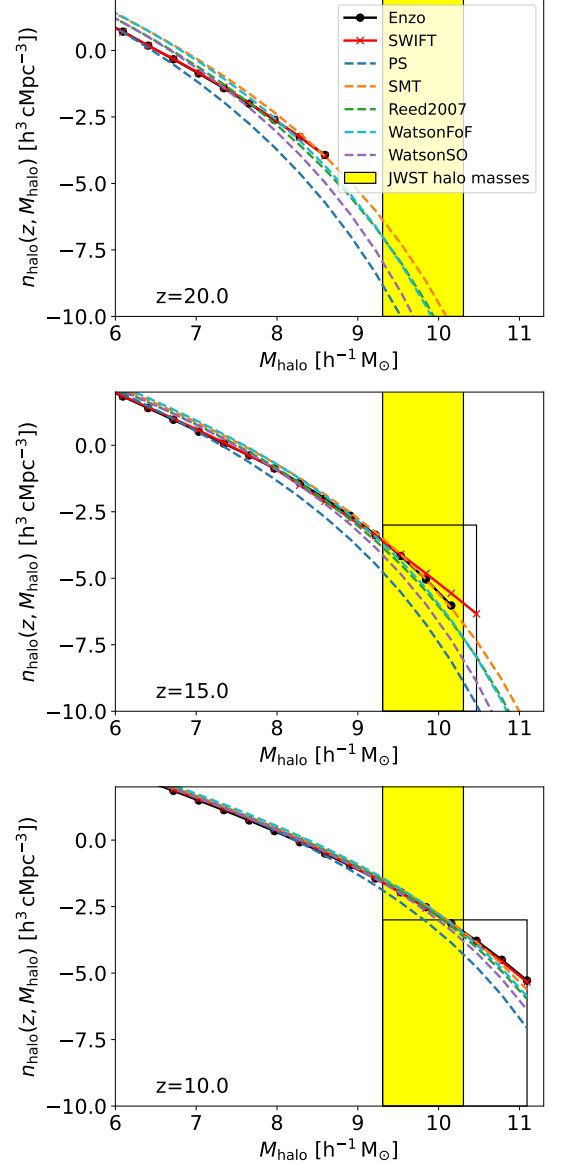


FIG. 2.— Comparing the Enzo and SWIFT halo number densities with five halo number densities derived from fits (see Table 4) at  $z = 20.0$  (upper panel),  $z = 15.0$  (centre panel) and  $z = 10.0$  (lower panel) using the FOF halo finder (with halo masses and number densities on a logarithmic scale). The black rectangles indicate the regions for more detailed analysis as seen in Figure 3. The yellow shaded regions represent the approximate range of halo masses detected by JWST at  $z \geq 10.0$ . Over the halo mass range selected at  $z = 10.0$ , all but the PS fit agree with numerical results within a factor of 2.

#### 2.4.2. Sheth, Mo & Tormen and Beyond

The Sheth, Mo & Tormen (2001) (SMT) halo mass function has a similar form to PS but assumes ellipsoidal collapse and is given as:

$$f_{\text{SMT}}(\sigma) = A \sqrt{\frac{2a}{\pi}} \left[ 1 + \left( \frac{\sigma^2}{a\delta_c^2} \right)^p \right] \frac{\delta_c}{\sigma} \exp\left(-\frac{a\delta_c^2}{2\sigma^2}\right), \quad (17)$$

where  $A = 0.3222$ ,  $a = 0.707$  and  $p = 0.3$ . We also test fitting functions developed by Reed et al. (2007) (Reed07) and Watson et al. (2013) (WatsonFoF refers to a fit using the Friends-of-Friends halo finder, Wat-

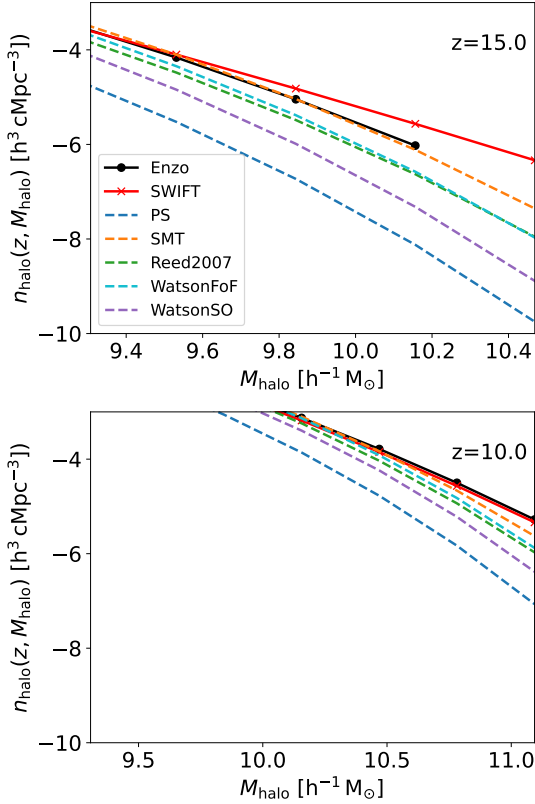


FIG. 3.— A zoom-in onto the black rectangles identified in Figure 2 (with halo masses and number densities on a logarithmic scale). These mass ranges represent the most massive halos accessible via numerical simulation at these redshifts. At this higher level of detail we see some discrepancy between the numerical halo mass functions of *Enzo* and *SWIFT* and their (semi-)analytical counterparts, particularly at  $z = 15.0$ . The residuals for each of the lines are shown in Figure 4 and Figure 5.

Fitting function	$z$ range	Reference
PS	No limit	<a href="#">Press &amp; Schechter (1974)</a>
SMT	No limit	<a href="#">Sheth, Mo &amp; Tormen (2001)</a>
Reed2007	0 - 30	<a href="#">Reed et al. (2007)</a>
WatsonFoF	0 - 30	<a href="#">Watson et al. (2013)</a>
WatsonSO	0 - 30	<a href="#">Watson et al. (2013)</a>

TABLE 4

THE FITTED HALO MASS FUNCTIONS WE USE TO COMPARE TO HMFs DERIVED FROM NUMERICAL SIMULATIONS.

sonSO refers to a fit using the Spherical Overdensity halo finder). The PS and SMT fits are widely-used and based on an analytical formalism, with no restriction on redshift or halo mass range. The Reed07, WatsonFoF and WatsonSO fits are based on simulation results, all with a redshift range of  $z \in (0, 30)$  and no explicit restriction on halo mass (see Table 4). While many other halo mass fitting functions exist, we choose these fits as they were all calibrated across the redshift range of interest to us (i.e.  $z > 10$ ). Other fitting functions are typically calibrated for lower redshifts.

We use the Python package *hmf* to compute halo number densities derived from the HMFs described above.

### 3. RESULTS

As previously stated, the goal of this paper is to compare halo number densities derived from simulation re-

sults with those derived from popular fits, and to test how well the fits can predict JWST halo mass abundances compared to simulations (e.g. [Boylan-Kolchin 2023](#)).

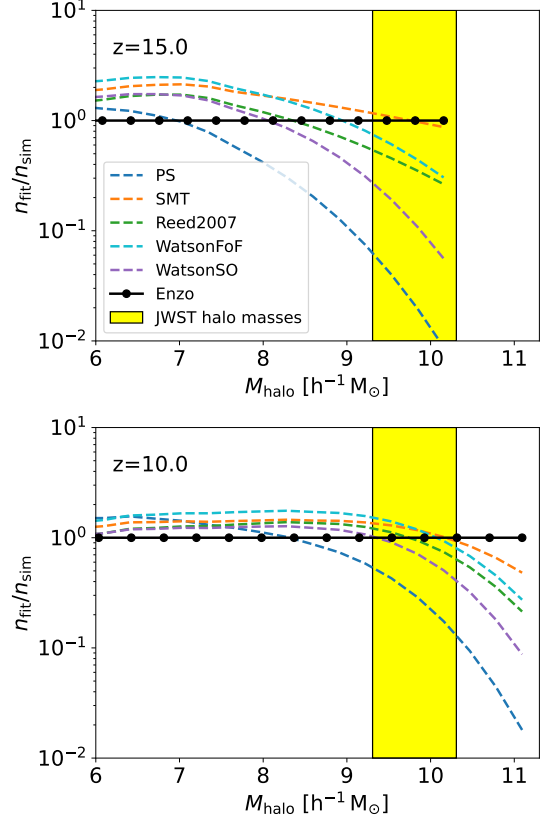


FIG. 4.— The ratios of the fitted halo number densities to the numerical halo number densities, derived from *Enzo* simulations and using the FOF halo finder (with halo masses on a logarithmic scale). Differences between *Enzo* and the (semi-)analytical HMFs are typically less than a factor of two at  $z = 10.0$  increasing to a factor of 5 at  $z = 15.0$  (excluding the PS fit).

In Figure 2, we compare the HMFs from *Enzo* and *SWIFT* data (dashed lines) with the chosen fits (solid lines) for  $z = 20.0$ ,  $z = 15.0$  and  $z = 10.0$  using the FOF halo finder. The black rectangles indicate the high mass range depicted in more detail in Figure 3. The range of halo masses selected in the black rectangles is bounded by the approximate lowest halo masses observable by JWST at these epochs up to the most massive halo masses accessible by the numerical simulations at that redshift. This is only possible for our outputs at  $z = 10.0$  and  $z = 15.0$  as halo masses large enough to be observed (except perhaps via extreme lensing) by JWST are simply not formed by  $z = 20.0$  in a  $\Lambda$ CDM universe. Hence, we focus our analysis on the  $z = 15.0$  and  $z = 10.0$  outputs in particular. Overlaid onto Figures 2 to 5 are yellow rectangles which act as a visual aid, depicting an estimate for the range of halo masses that host recently-observed JWST galaxies and galaxy candidates. We choose sources with  $10.0 < z < 15.0$ <sup>2</sup> and with an estimate of  $M_*$  or  $M_{\text{halo}}$  available. These sources include GN-z11 ([Scholtz et al. 2024](#)), Maisie’s Galaxy ([Arrabal](#)

<sup>2</sup> We use photometric redshift only if spectroscopic redshift is not yet available.

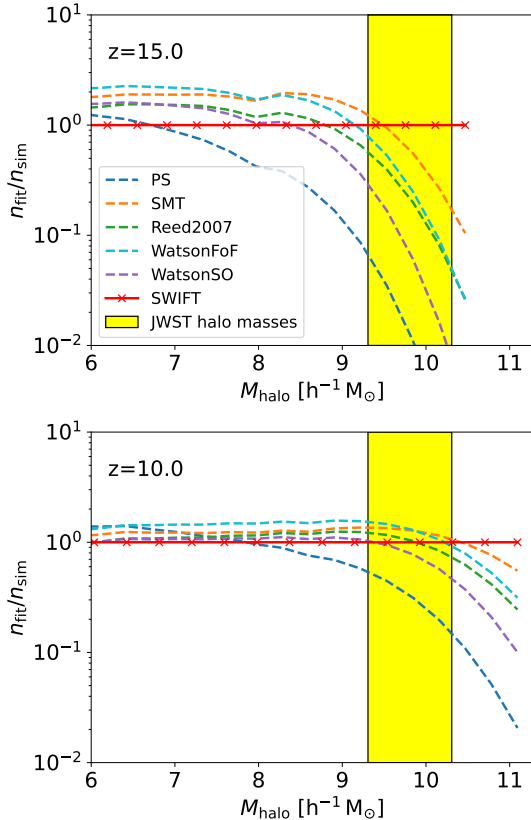


FIG. 5.— The ratios of the fitted halo number densities to the numerical halo number densities, derived from *SWIFT* simulations and using the FOF halo finder (with halo masses on a logarithmic scale). Similar to the *Enzo* result, *SWIFT* shows excellent agreement with the (semi-) analytic HMFs, all fits except PS agreeing within a factor of 2 for all but the highest masses at  $z = 10.0$ . There is a greater discrepancy present at  $z = 15.0$ , with some fits underestimating the numerical results by a factor of 100 at the high-mass range.

Haro et al. 2023b), GS-z14 (Helton et al. 2024) and others (Chakraborty et al. 2024). If there exists no estimate of  $M_{\text{halo}}$  yet for a given source, we estimate it using the following equation:

$$M_{\text{halo}}(z, M_*) = \frac{\Omega_m(z)}{\Omega_b(z)} \frac{M_*}{\epsilon_*}, \quad (18)$$

where we set the star formation efficiency parameter  $\epsilon_* = 0.1$ . The width of the yellow rectangle is determined by the minimum and maximum halo masses in our sample and does not vary with redshift due to the small number of sources. In Figures 4 and 5, we take the ratios of the semi-analytic halo number densities against the *Enzo* and *SWIFT* outputs respectively to quantify the overall disagreements at  $z = 10.0$  and  $z = 15.0$ .

Over the full mass range, for both simulation suites and halo finders, we find the fits considered agree well across the entire spectrum. There is, over several dexes in mass and over the redshift range between  $z = 10.0$  and  $z = 20.0$ , excellent agreement between all of the HMFs. Additionally, the fits improve as redshift decreases - not just between the numerical results and the (semi-)analytic results but even among the (semi-)analytic fits themselves.

At the lower mass range ( $10^6$  to  $10^7 h^{-1} M_\odot$ ), the

semi-analytic fits overestimate the halo number densities by up to a factor of  $\approx 2$  compared to either *Enzo* or *SWIFT* data.

At the mid-range masses ( $10^7$  to  $10^9 h^{-1} M_\odot$ ) at  $z = 10.0$ , all but the PS fit overestimate the numerical simulations by less than a factor of 2. This is best illustrated by the bottom panels of Figures 4 and 5. For the same mass range at  $z = 15.0$ , there is a greater discrepancy with all but the SMT and WatsonFOF fits underestimating the halo number densities by up to a factor of  $\approx 5$  compared to numerical simulations (see the top panels of Figures 4 and 5).

In the JWST mass range, we see the greatest discrepancies. At  $z = 15.0$ , the PS semi-analytic fit underestimates the *Enzo* halo number density by a factor of  $\approx 100$  (see Figure 4 (top panel)). The other fits agree within a factor of  $\approx 50$  (WatsonSO) in the worst case with the SMT fit providing the closest match. We see a similar story at  $z = 10.0$  with a less extreme discrepancy (PS underestimating by a factor of  $\approx 10$ , the other fits agreeing within a factor of  $\approx 2$  (see Figure 4 (bottom panel))). This is consistent with the results and conclusions of Yung et al. (2024).

For the *SWIFT* simulations at  $z = 15.0$ , we see a strong deviation towards higher masses which was not present for the *Enzo* simulations (see Figure 5 (top panel)). Both PS and WatsonSO underestimate the numerical halo number densities by a factor of  $\approx 100$ , and SMT agrees best within a factor of  $\approx 10$ . It appears here that the *Enzo* runs are better able to resolve halos at earlier times perhaps due to the inherent refinement strategy. A detailed analysis of the difference between the numerical codes is outside the scope of this paper and comparisons in this direction have been undertaken in the past (e.g. O’Shea et al. 2005; Regan, Haehnelt & Viel 2007; Hayward et al. 2014). At  $z = 10.0$  the agreement between the numerical (*SWIFT*) results and the analytic fits remains excellent (see Figure 5 (bottom panel)). The PS fit underestimates the numerical results by a factor of  $\approx 10$ , with the other fits agreeing within a factor of 2. In Figure 3 (top panel), we see a discrepancy between the *Enzo* and *SWIFT* results in the high-mass range at  $z = 15.0$ . Previous work (e.g. Warren et al. 2006; More et al. 2011) has shown that the FOF mass is sensitive to mass resolution and the presence of substructure, which will be strongly dependent on redshift and which is difficult to correct for in general. It will also depend on local clustering, which can lead to distinct structures being linked by bridges of particles. This is the most likely explanation for the variance between *Enzo* and *SWIFT* at  $z = 15.0$ . Note that this variance is absent from the HOP profiles (see Figure A.2).

In summary the agreement between the numerical N-body solvers and the (semi-)analytic fits is excellent. In particular, the SMT fitting function gives excellent agreement with *Enzo*, with deviations of at most approximately a factor of 2 at  $z = 15.0$  (for low halo masses which are anyway currently unobservable) and converging to much less than a factor of two within the JWST window at  $z = 10.0$ . For *SWIFT*, the agreement with SMT is equally excellent at  $z = 10.0$  but deviates somewhat for the higher halo masses at  $z = 15.0$ . Using such (semi-)analytic fits, then, is unlikely to be a dominant source of error when testing high redshift observations

against  $\Lambda$ CDM models.

#### 4. DISCUSSION

The recent explosion of data from the high- $z$  Universe, particularly beyond  $z = 10$ , by JWST has led to a number of claims that the data is in tension with our galaxy formation and cosmological models (e.g. [Boylan-Kolchin 2023](#); [Arrabal Haro et al. 2023a](#); [Yung et al. 2024](#); [Finkelstein et al. 2024](#)). The Universe beyond  $z = 10$  however is likely to be significantly different to the later and present-day Universe. At  $z \gtrsim 10$ , galaxies are still in their infancy, with the most massive galaxies at those epochs having stellar masses less than  $10^{10} M_{\odot}$  (these would be classified as dwarfs in the present-day Universe). Moreover, there is strong evidence that the astrophysical processes at play at  $z = 10$  are sufficiently different to those of the present-day Universe and that they make significant alterations to the galaxy properties. This is particularly evident in galaxies like GN-z11 which is thought to harbour a massive black hole at its centre ([Maiolino et al. 2024b](#)), moreover this galaxy contains species abundances which are difficult to explain through standard processes (e.g. [Bunker et al. 2023](#); [Cameron et al. 2023](#); [Charbonnel et al. 2023](#); [Nandal et al. 2024](#)). This peculiarity and lack-of-understanding is not unique to GN-z11 with a number of galaxies displaying properties which has evoked confusion within the community (e.g. [Maiolino et al. 2024a](#)). The most luminous galaxies observed by JWST remain in tension with state-of-the-art cosmological simulations (e.g. [Keller et al. \(2023\)](#)) with simulations struggling to model their extreme brightness at very early times. The reasons behind this are currently unknown but a greater emphasis on processes specific to the early Universe such as population III star formation and early black hole formation (e.g. [McCaffrey et al. \(2023\)](#)) may offer a pathway forward. It has also been argued that this tension may be resolved with the use of high-resolution simulations targeted at the high-redshift universe (see [McCaffrey et al. \(2023\)](#)).

A key part of making progress in understanding the high- $z$  Universe is therefore to identify sources of systematic error in our models at high- $z$ . Some sources of uncertainty in counting galaxies at such redshifts include cosmic variance (especially significant at the distances considered), error in stellar mass estimation and the presence of backplash halos (halos that have lost some dark matter from the host halo, giving the impression of a higher baryon-dark matter ratio). These uncertainties have been explored thoroughly by [Chen, Mo & Wang \(2023\)](#). In this paper we focus on exploring differences in fitting functions to the universal HMF and how they compare against direct N-body simulations at  $z \geq 10$ . In particular, we compare a wide range of fitting functions in use in the literature (see Table 4) against the adaptive mesh refinement code *Enzo* and against the N-body SPH code *SWIFT*.

We find that, for both *Enzo* and *SWIFT*, the match against the HMF (semi-)analytic functions is excellent, with many fits agreeing with numerical results within a factor of 2 for low and mid-range halo masses. The match against the standard [Press & Schechter \(1974\)](#) formalism is less accurate with deviations of up to an order of magnitude (at  $z = 10.0$  and  $z = 15.0$ ). Similarly, when comparing against standard fitting formula (see Table 4)

we again see good agreement with deviations typically within an order of magnitude up to  $z = 15.0$  inside the window in which JWST can approximately observe high- $z$  galaxies.

We caution that the spatial resolution employed, controlled via the softening parameter for *SWIFT* and via the level of maximum refinement with *Enzo*, is set relatively high for our simulations. For example, we use a softening length set to approximately the mean inter-particle spacing divided by 25. This is slightly lower than the resolution we evolve the *Enzo* simulations with. This level of gravity resolution, specifically the softening length and spatial resolution here, is likely to be significantly higher than that used for typical galaxy formation simulations designed to run to  $z \sim 0$  (e.g. [Power et al. 2003, 2016](#); [Zhang et al. 2019](#)). It is also worth noting that the gravitational collapse of dark matter halos is sensitive to the large-scale gravitational field, which in a numerical simulation depends on the size of the simulation volume. Previous work (e.g. [Power & Knebe 2006](#)) has highlighted how the mass function is sensitive to simulation volume, with a deficit of halos of a given mass at high masses. This effect is most pronounced in studies of the mass function at high redshifts, where the necessary high mass resolutions and large simulation volumes make these simulations particularly challenging. We therefore caution the reader that matching the results from numerical simulations designed primarily for large-scale investigations may struggle to calculate the correct halo properties and abundances at  $z \gtrsim 10$  (see e.g. [Keller et al. 2023](#)) unless the simulations are truly focused on high- $z$  study (see e.g. [McCaffrey et al. 2023](#)).

Nonetheless, overall we find excellent agreement between N-body simulations and both (semi-)analytic and fitting functions to HMFs, consistent with the results from [Yung et al. \(2024\)](#), and that these functions are unlikely to lead to large errors in our modelling of high- $z$  host halos when appropriately modelled.

#### DATA AVAILABILITY

The analysis code used to produce the figures shown here is available upon request.

#### ACKNOWLEDGEMENTS

JR acknowledges support from the Royal Society and Science Foundation Ireland under grant number URF\R1\191132 and support from the Irish Research Council Laureate programme under grant number IRC\LA/2022/1165. CP acknowledges the support of the Australian Research Council Centre of Excellence for All Sky Astrophysics in 3 Dimensions (ASTRO 3D), through project number CE170100013. HOB thanks JR's research group for many helpful discussions and insights: John Brennan, Lewis R. Prole, Saoirse Ward, Joe McCaffrey, Pelle van de Bor and Daxal Mehta. The authors wish to acknowledge the Irish Centre for High-End Computing (ICHEC) for the provision of computational facilities and support via the Meluxina facility, hosted by LuxProvide (Luxembourg). We wish to thank the EuroHPC Joint Undertaking for awarding this project access to the EuroHPC supercomputer Karolina, hosted by IT4I (Czech Republic) through a EuroHPC Regular Access call. We also thank the anonymous referee for a constructive and insightful report.



## REFERENCES

- Arrabal Haro P. et al., 2023a, *Nature*, 622, 707  
 Arrabal Haro P. et al., 2023b, *Nature*, 622, 707  
 Boylan-Kolchin M., 2023, *Nature Astronomy*, 7, 731  
 Brummel-Smith C. et al., 2019, *The Journal of Open Source Software*, 4, 1636  
 Bryan G. L., Norman M. L., 1998, *The Astrophysical Journal*, 495, 80–99  
 Bryan G. L., et al., 2014, *The Astrophysical Journal Supplement Series*, 211, 19, publisher: IOP ADS Bibcode: 2014ApJS..211...19B  
 Bunker A. J., et al., 2023, *Astronomy & Astrophysics*, 677, A88  
 Cameron A. J., Katz H., Rey M. P., Saxena A., 2023, *MNRAS*, 523, 3516  
 Castellano M. et al., 2024, arXiv e-prints, arXiv:2403.10238  
 Chakraborty P., Sarkar A., Wolk S., Schneider B., Brickhouse N., Lanzetta K., Foster A., Smith R., 2024, arXiv e-prints, arXiv:2406.05306  
 Charbonnel C., Schaerer D., Prantzos N., Ramírez-Galeano L., Fragos T., Kuruvanthodi A., Marques-Chaves R., Gieles M., 2023, *A&A*, 673, L7  
 Chen Y., Mo H. J., Wang K., 2023, *MNRAS*, 526, 2542  
 Cheng H., Greengard L., Rokhlin V., 1999, *Journal of Computational Physics*, 155, 468  
 Efstathiou G., Davis M., White S. D. M., Frenk C. S., 1985, *The Astrophysical Journal Supplement Series*, 57, 241, publisher: IOP ADS Bibcode: 1985ApJS...57..241E  
 Eisenstein D. J., Hu W., 1998, *The Astrophysical Journal*, 496, 605, publisher: IOP ADS Bibcode: 1998ApJ...496..605E  
 Eisenstein D. J., Hut P., 1998, *The Astrophysical Journal*, 498, 137, publisher: IOP ADS Bibcode: 1998ApJ...498..137E  
 Finkelstein S. L. et al., 2024, *ApJ*, 969, L2  
 Frigo M., Johnson S., 2005, *Proceedings of the IEEE*, 93, 216  
 Gentile F. et al., 2024, arXiv e-prints, arXiv:2408.10305  
 Hahn O., Abel T., 2011, *Monthly Notices of the Royal Astronomical Society*, 415, 2101, arXiv:1103.6031 [astro-ph]  
 Hainline K. N. et al., 2024, arXiv e-prints, arXiv:2404.04325  
 Harikane Y., Nakajima K., Ouchi M., Umeda H., Isobe Y., Ono Y., Xu Y., Zhang Y., 2024, *ApJ*, 960, 56  
 Hayward C. C., Torrey P., Springel V., Hernquist L., Vogelsberger M., 2014, *MNRAS*, 442, 1992  
 Helton J. M. et al., 2024, arXiv e-prints, arXiv:2405.18462  
 Kannan R. et al., 2023, *MNRAS*, 524, 2594  
 Keller B. W., Munshi F., Trebitsch M., Tremmel M., 2023, *ApJ*, 943, L28  
 Knebe A. et al., 2011, *MNRAS*, 415, 2293  
 Labbé I. et al., 2023, *Nature*, 616, 266  
 Lacey C., Cole S., 1994, *Monthly Notices of the Royal Astronomical Society*, 271, 676–692  
 Lu S., Frenk C. S., Bose S., Lacey C. G., Cole S., Baugh C. M., Helly J. C., 2024, arXiv e-prints, arXiv:2406.02672  
 Lukić Z., Heitmann K., Habib S., Bashinsky S., Ricker P. M., 2007, *ApJ*, 671, 1160  
 Maiolino R. et al., 2024a, arXiv e-prints, arXiv:2405.00504  
 Maiolino R. et al., 2024b, *Nature*, 627, 59  
 McCaffrey J., Hardin S., Wise J. H., Regan J. A., 2023, *The Open Journal of Astrophysics*, 6, 47  
 Monaghan J. J., Lattanzio J. C., 1985, *A&A*, 149, 135  
 More S., Kravtsov A. V., Dalal N., Gottlöber S., 2011, *ApJS*, 195, 4  
 Murray S. G., Power C., Robotham A. S. G., 2013, *Astronomy and Computing*, 3, 23, aDS Bibcode: 2013A&C....3...23M  
 Nandal D., Regan J. A., Woods T. E., Farrell E., Ekström S., Meynet G., 2024, *A&A*, 683, A156  
 O’Shea B. W., Nagamine K., Springel V., Hernquist L., Norman M. L., 2005, *ApJS*, 160, 1  
 Power C., Knebe A., 2006, *MNRAS*, 370, 691  
 Power C., Navarro J. F., Jenkins A., Frenk C. S., White S. D. M., Springel V., Stadel J., Quinn T., 2003, *MNRAS*, 338, 14  
 Power C., Robotham A. S. G., Obreschkow D., Hobbs A., Lewis G. F., 2016, *MNRAS*, 462, 474  
 Press W. H., Schechter P., 1974, *The Astrophysical Journal*, 187, 425, publisher: IOP ADS Bibcode: 1974ApJ...187..425P  
 Reed D. S., Bower R., Frenk C. S., Jenkins A., Theuns T., 2007, *Monthly Notices of the Royal Astronomical Society*, 374, 2, publisher: OUP ADS Bibcode: 2007MNRAS.374....2R  
 Regan J. A., Haehnelt M. G., Viel M., 2007, *MNRAS*, 374, 196  
 Rennehan D., 2022, yt-swift/yt at main · rennehan/yt-swift  
 Rennehan D., 2024, arXiv e-prints, arXiv:2406.06672  
 Schaller M., Gonnet P., Draper P. W., Chalk A. B. G., Bower R. G., Willis J., Hausammann L., 2018, *Astrophysics Source Code Library*, ascl:1805.020, aDS Bibcode: 2018ascl.soft05020S  
 Schaller M., et al., 2024, *Monthly Notices of the Royal Astronomical Society*, publisher: OUP ADS Bibcode: 2024MNRAS.tmp..925S  
 Scholtz J. et al., 2024, *A&A*, 687, A283  
 Sheth R. K., Mo H. J., Tormen G., 2001, *Monthly Notices of the Royal Astronomical Society*, 323, 1  
 Sheth R. K., Tormen G., 1999, *MNRAS*, 308, 119  
 Skory S., Turk M. J., Norman M. L., Coil A. L., 2010, *ApJS*, 191, 43  
 Smith B. et al., 2022, yt-project/yt\_astro\_analysis: yt\_astro\_analysis version 1.1.1 is released!  
 Springel V., 2005, *MNRAS*, 364, 1105  
 Steinhardt C. L., Kokorev V., Rusakov V., Garcia E., Sneppen A., 2023, *ApJ*, 951, L40  
 Sun G., Faucher-Giguère C.-A., Hayward C. C., Shen X., Wetzel A., Cochrane R. K., 2023, *ApJ*, 955, L35  
 Turk M. J., Smith B. D., Oishi J. S., Skory S., Skillman S. W., Abel T., Norman M. L., 2011, *The Astrophysical Journal Supplement Series*, 192, 9, publisher: IOP ADS Bibcode: 2011ApJS..192....9T  
 Warren M. S., Abazajian K., Holz D. E., Teodoro L., 2006, *ApJ*, 646, 881  
 Watson W. A., Iliev I. T., D’Aloisio A., Knebe A., Shapiro P. R., Yepes G., 2013, *Monthly Notices of the Royal Astronomical Society*, 433, 1230–1245  
 Yung L. Y. A., Somerville R. S., Nguyen T., Behroozi P., Modi C., Gardner J. P., 2024, *MNRAS*, 530, 4868  
 Zhang T., Liao S., Li M., Gao L., 2019, *MNRAS*, 487, 1227

## APPENDIX

## ALTERNATIVE HALO FINDING TECHNIQUES

In addition to the widely-used Friends-of-Friends halo finding algorithm, we also investigate how a different halo finder would impact our results. As discussed in §2 we also use the HOP halo finder (Eisenstein & Hut (1998)) in our analysis. In Figures A.1 to A.4, we reproduce Figures 2 to 5 from the main text respectively but with the halo finding technique switched to HOP instead of FOF. Using the HOP halo finder we find near identical results to the FOF method and again we see approximately a factor of two difference between HOP and the analytic HMFs at both  $z = 10.0$  and  $z = 15.0$ . The difference between HOP and the fitting functions varies up to an order of magnitude but similar to the FOF method the agreement is nonetheless still very good - particularly at  $z = 10.0$  where differences are typically less than a factor of two. We see negligible differences between FOF and HOP - a finding supported by other research studies (Knebe et al. 2011).

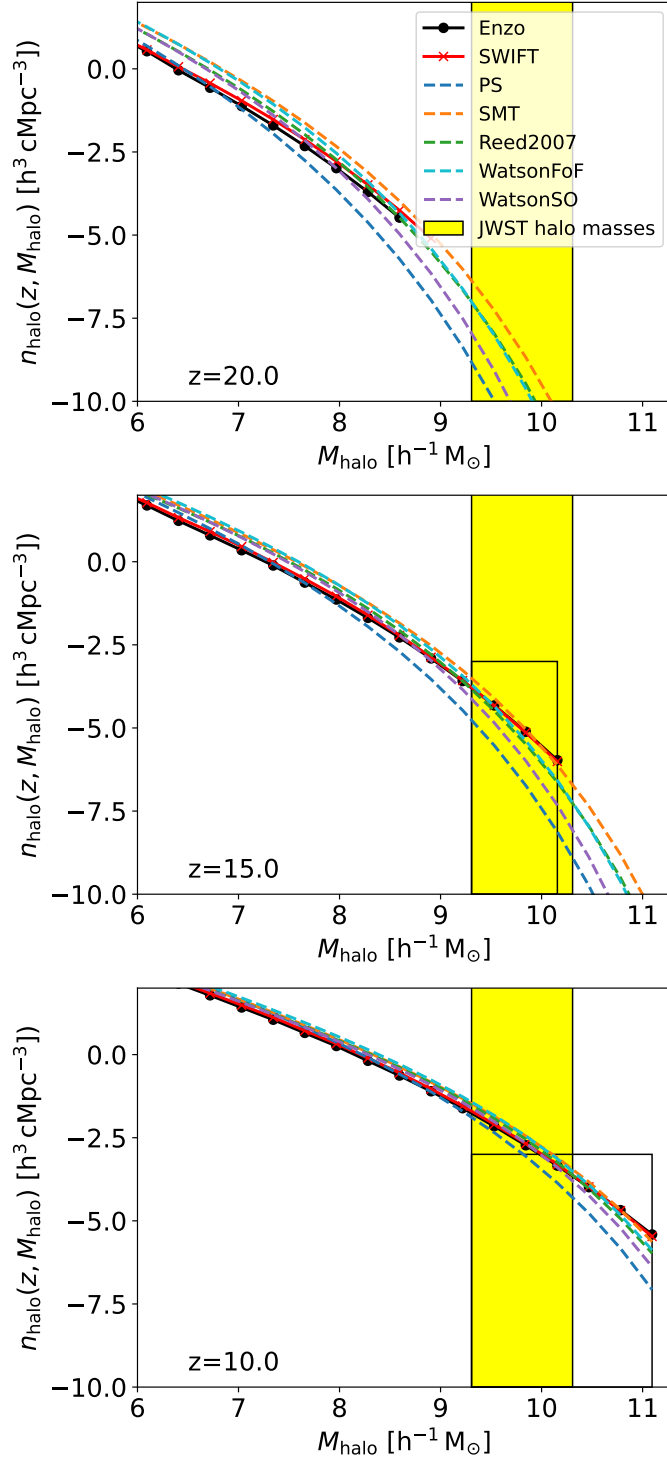


FIG. A.1.— Comparing the **Enzo** and **SWIFT** halo number densities contrasted with 5 halo number densities derived from fits at  $z = 20.0$  (upper panel),  $z = 15.0$  (centre panel) and  $z = 10.0$  (bottom panel) using the HOP halo finder (with halo masses and number densities on a logarithmic scale).

This paper was built using the Open Journal of Astrophysics L<sup>A</sup>T<sub>E</sub>X template. The OJA is a journal which provides fast and easy peer review for new papers in the **astro-ph** section of the arXiv, making the reviewing process simpler for authors and referees alike. Learn more at <http://astro.theoj.org>.

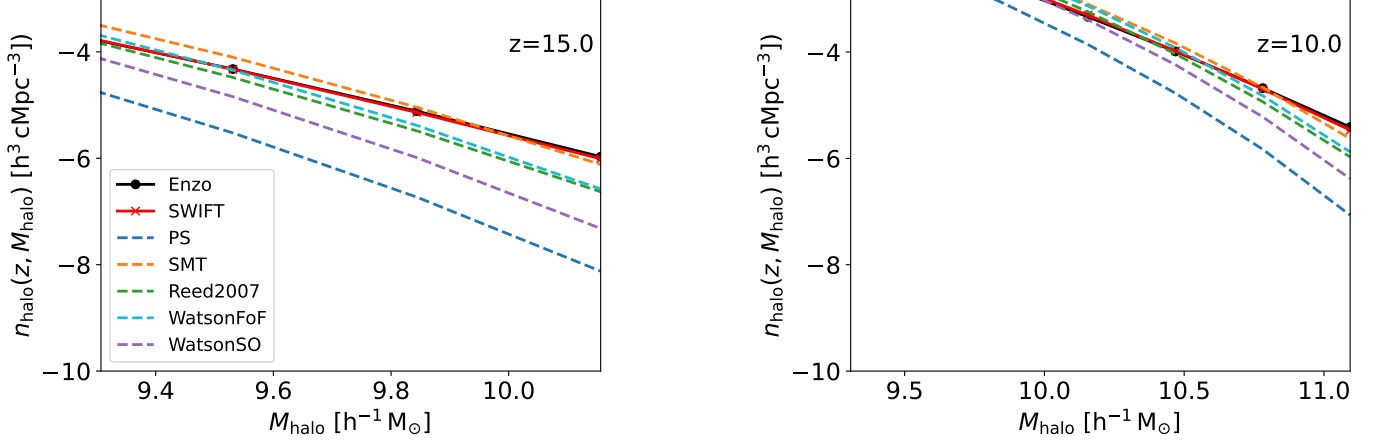


FIG. A.2.— High-mass sections of Figure A.1 (centre and bottom panels) shown in more detail.

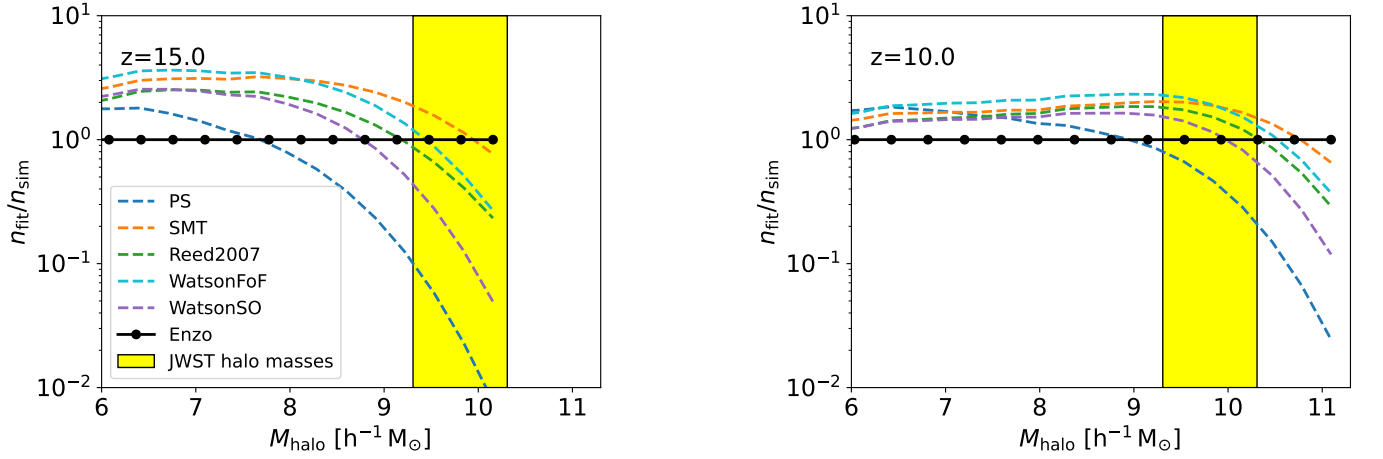


FIG. A.3.— The ratios of the fitted halo number densities to the numerical halo number densities, derived from **Enzo** simulations and using the HOP halo finder (with halo masses on a logarithmic scale).

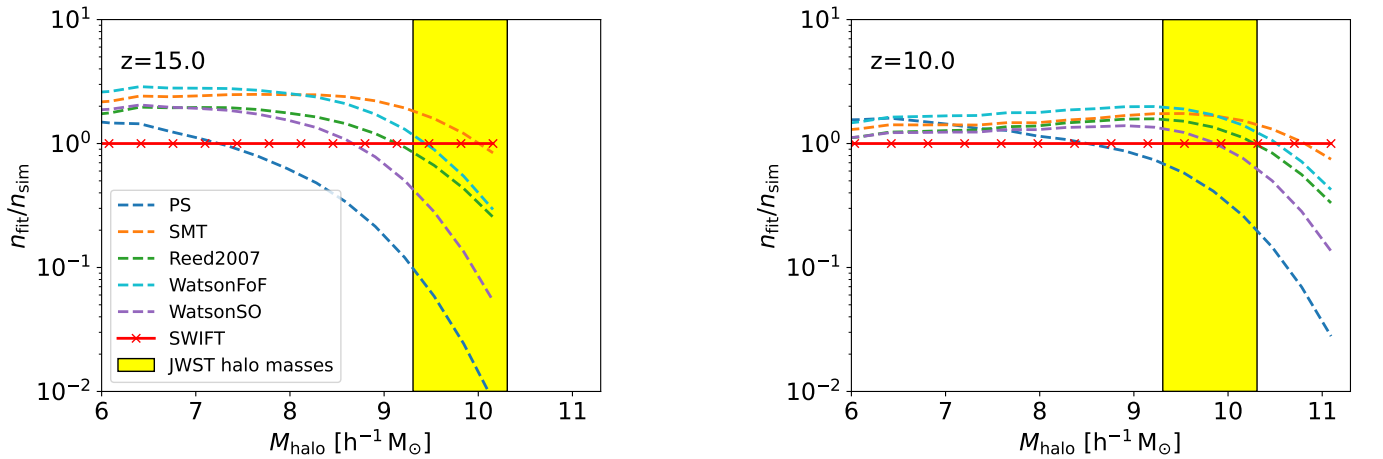


FIG. A.4.— The ratios of the fitted halo number densities to the numerical halo number densities, derived from **SWIFT** simulations and using the HOP halo finder (with halo masses on a logarithmic scale).